ACS APPLIED MATERIALS & INTERFACES

Research Article

www.acsami.org

Compositional Engineering of Perovskite Oxides for Highly Efficient Oxygen Reduction Reactions

Dengjie Chen,[†,‡,§,#] Chi Chen,[§,#] Zhenbao Zhang,[†,‡] Zarah Medina Baiyee,[§] Francesco Ciucci,*[,§,⊥] and Zongping Shao*[,†,‡]

[†]State Key Laboratory of Materials-Oriented Chemical Engineering, Nanjing Tech University, Nanjing 210009, China

[‡]College of Chemistry & Chemical Engineering, Nanjing Tech University, Nanjing 210009, China

[§]Department of Mechanical and Aerospace Engineering, The Hong Kong University of Science and Technology, Hong Kong, China

[⊥]Department of Chemical and Biomolecular Engineering, The Hong Kong University of Science and Technology, Hong Kong, China

ABSTRACT: Mixed conducting perovskite oxides are promising catalysts for high-temperature oxygen reduction reaction. Pristine $SrCoO_{3-\delta}$ is a widely used parent oxide for the development of highly active mixed conductors. Doping a small amount of redox-inactive cation into the B site (Co site) of $SrCoO_{3-\delta}$ has been applied as an effective way to improve physicochemical properties and electrochemical performance. Most findings however are obtained only from experimental observations, and no universal guidelines have been proposed. In this article, combined experimental and theoretical studies are conducted to obtain fundamental understanding of the effect of B-site doping concentration with redox-inactive cation (Sc) on the properties and performance of the perovskite oxides. The phase structure, electronic conductivity, defect chemistry, oxygen reduction kinetics, oxygen ion transport, and electrochemical reactivity are experimentally characterized. In-depth analysis of doping level effect is also undertaken by first-principles calculations. Among the compositions, $SrCo_{0.95}Sc_{0.05}O_{3-\delta}$ shows the best oxygen kinetics and corresponds to the minimum fraction of Sc for stabilization of the oxygen-vacancy-disordered structure. The results strongly support that B-site doping of $SrCoO_{3-\delta}$ with a small amount of redox-inactive cation is an effective strategy toward the development of highly active mixed conducting perovskites for efficient solid oxide fuel cells and oxygen transport membranes.

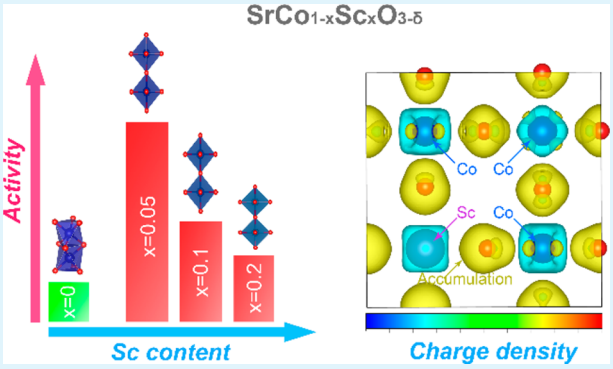

KEYWORDS: *$SrCoO_{3-\delta}$, compositional engineering, oxygen reduction kinetics, solid oxide fuel cells, oxygen transport membranes, first-principles calculations*

INTRODUCTION

Mixed ionic and electronic conducting (MIEC) perovskite oxides have been developed to possess good catalytic activity, structural flexibility, and chemical stability. These properties position the materials at the forefront of high-temperature energy technologies, including gas sensors, solid oxide fuel cells (SOFCs), oxygen transport membranes (OTMs), and membrane reactors.[1−5] The composition and doping flexibility of perovskite materials enables vast property tailoring to meet specific requirements for various applications.[6−8] Among the numerous MIEC perovskites, the $SrCoO_{3-\delta}$ series have shown a notably high oxygen nonstoichiometry and structural flexibility, resulting from both the extrinsic dopants and the outstanding redox capabilities of the transition-metal ion Co.

It has been previously shown that pristine $SrCoO_{3-\delta}$ tends to form an oxygen-vacancy-ordered perovskite structure. This type of structure deactivates the long-range oxygen transport and results in a relatively high area-specific resistance when adopted as cathodes for SOFCs, and low oxygen permeation fluxes when applied as materials for OTMs.[9−11] Simultaneous A- and B-site substituting of $SrCoO_3$ has led to the development of barium strontium cobalt iron oxide (BSCF), one of the most widely studied cathode materials for SOFCs.[12−14] Although promising catalytic activities have been demonstrated, widespread applications of BSCF are hampered by the relatively low structural and chemical stability at low temperature and low oxygen partial pressure.[15−17] It is therefore imperative to investigate the factors that govern the stability and activity so as to improve the material's design in oxygen reduction catalysts.[18,19]

Recently, it was experimentally shown that substituting the reducible Co site (B site) with a modest amount of cation with a fixed valence state, such as Nb^{5+}, Ta^{5+}, Ti^{4+}, and Sc^{3+}, can stabilize the oxygen-disordered perovskite structure of $SrCoO_{3-\delta}$.[10,20−29] Aguadero et al. systematically investigated the $SrCo_{1-x}Sb_xO_{3-\delta}$ and $SrCo_{1-x}Mo_xO_{3-\delta}$ series and found that

Received: January 13, 2015
Accepted: April 7, 2015
Published: April 7, 2015

DOI: 10.1021/acsami.5b00358
ACS Appl. Mater. Interfaces 2015, 7, 8562−8571

B-site doping of Sb and Mo elements resulted in either a tetragonal $P4/mmm$ or cubic $Pm\bar{3}m$ structure, depending on the substitution fraction.[20,21] These stabilized materials showed outstanding performance as SOFC cathodes and OTMs. In particular, the Shao group demonstrated a peak power density as high as 902 mW cm^{-2} at 600 °C for $SrSc_{0.2}Co_{0.8}O_{3-\delta}$ cathodes in SOFCs.[30] The same group obtained an oxygen flux as high as 3.1 mL cm^{-2} min^{-1} at 900 °C with the $SrSc_{0.05}Co_{0.95}O_{3-\delta}$ membrane among a series of $SrM_{0.05}Co_{0.95}O_{3-\delta}$ (M = Bi, Zr, Ce, Sc, La, Y, Al, and Zn).[24] The excellent oxygen ion transport and electrochemical activities were attributed to the stabilization of a vacancy-disordered structure, which enables 3D transport pathways for oxygen ions. Interestingly, the authors found that structure could be effectively stabilized for doping as low as 5%.

Up to now, the effect of the doping element and the determination of the optimal substitution level has been obtained experimentally, while a fundamental understanding of the structural stabilization and improved performance from the B-site doping is still missing. Theoretical studies based on first-principles calculations of the $SrMO_3$ (M = Sc, Ti, V, Cr, Mn, Fe, Co, Ni, Zn, Ga, Ge, As, Zr, Nb, Mo, Tc, Ru, Rh, Pd, Cd, In, Sn, and Sb) series elucidated a general correlation for the B-site cation and oxygen migration energy barrier.[31] This demonstrates that the theoretical tools may also be employed for a comprehensive analysis of B-site doped $SrCoO_{3-\delta}$. Furthermore, a fundamental understanding of this behavior may reveal new trends and more universal rules for better material design of MIEC perovskites.

This work aims to provide insight into the general effects of doping level of redox-inactive cation (Sc) at the B site on $SrCoO_{3-\delta}$. Sc has been adopted as a model material due to its promising effectiveness in $SrCoO_{3-\delta}$-based compositions.[24] Employing both systematic experimental studies and first-principles calculations based on density functional theory (DFT), this work identifies the effects of doping level of B-site dopant on the structure, defect chemistry, electrical and electrochemical properties, and oxygen exchange kinetics of the Sc doped $SrCoO_{3-\delta}$. The results are further analyzed in relation to the material performance as cathodes in SOFCs and materials for OTMs. The relation of concentration of B-site dopant (Sc) on the above properties and the electrochemical performance as obtained in this study is considered to be universal and therefore transferable for high-temperature oxygen catalyst design.

EXPERIMENTAL SECTION

Powder Synthesis. The $SrCo_{1-x}Sc_xO_{3-\delta}$ (x = 0, 0.05, 0.1, and 0.2) oxides were synthesized via solid-state reaction instead of the sol−gel process.[9,32] This method was undertaken to both simplify the procedure and to gain further information in respect to the effect of preparation method on materials' properties and performance. Stoichiometric amounts of $SrCO_3$, Sc_2O_3, and Co_2O_3 (analytical grade, Sinopharm Chemical Reagent Co., Ltd.) were mixed by grinding. This was carried out using a high-energy ball miller (Pulverisette, 6 Fritsch) in a liquid ethanol medium at 400 rpm for 1 h. After drying, the powders were pressed and calcined at 1000 °C for 10 h. The milling, pressing, and calcination processes were repeated twice.

Membrane Fabrication. Dense membranes with relative densities of higher than 95% were prepared for the oxygen permeation test by dry pressing as-synthesized powders and high-temperature sintering at 1100 °C for 5 h. After sintering and polishing, the dimensions of membranes were ∼12 mm in diameter and ∼1 mm in thickness.

Symmetrical Cell Fabrication. Symmetrical cells with $SrCo_{1-x}Sc_xO_{3-\delta}$ electrodes (∼200 nm) on both sides of the $Sm_{0.2}Ce_{0.8}O_{1.9}$ (SDC) electrolyte, i.e. an electrode|SDC|electrode configuration, were prepared using pulsed laser deposition (PLD, Neocera JP-788). The $SrCo_{1-x}Sc_xO_{3-\delta}$ targets for the PLD were also prepared by dry pressing the as-synthesized powders and then high-temperature sintering. Before deposition, the surface of the target was polished and ablated. The deposition parameters are identical to those reported in the previous publications.[33,34] After deposition and annealing at 700 °C for 45 min in the PLD chamber, the electrode|SDC|electrode symmetrical cells were further annealed at 1000 °C for 2 h in air. Silver paste (DAD-87, Shanghai Research Institute of Synthetic Resins, Shanghai, China) was printed on the electrode surfaces as a current collector.

Characterizations. The crystal structures of the $SrCo_{1-x}Sc_xO_{3-\delta}$ powders were characterized at room temperature by X-ray diffraction (XRD, D8 Advance, Bruker) using Cu Kα radiation at 40 kV and 40 mA. The diffraction patterns were collected at the scan rate of 0.02° per step. Rietveld refinement on the tested XRD patterns was conducted using the Fullprof Suite program. General parameters such as the scale factor, zero point, background parameters with six-coefficients polynomial function, lattice parameters, and peak shapes with the description by Thompson−Cox−Hastings profiles were optimized.

The cation stoichiometries of the prepared $SrCo_{1-x}Sc_xO_{3-\delta}$ powders were measured by inductively coupled plasma emission spectroscopy (ICP; PerkinElmer OPTIMA 2000). The compositions at the surface were analyzed by X-ray photoelectron spectroscopy (XPS, PHI 5600) with Al monochromatic X-rays at a power of 150 W. The depth profiling XPS was carried out to provide the composition information on $SrCo_{1-x}Sc_xO_{3-\delta}$ thin films from the surface to the bulk with the reference sputtering rate of 0.35 Å s^{-1} for SiO_2.

The iodometric titration method was used to quantify the oxygen content at room temperature in the $SrCo_{1-x}Sc_xO_{3-\delta}$ oxides. Approximately 100 mg of the powder was dissolved in dilute HCl with the presence of KI in excess as a reductant to reduce high-valence reducible metal ions (Co^{3+}, Co^{4+}). To avoid the oxidation of I^- by air, the solution was put under the protection of a nitrogen atmosphere. I_2 was finally titrated by a standard $S_2O_3^{2-}$ solution using starch as indicator to determine the average valence state of the Co ion.

The electronic conductivity was measured using the four-probe direct current technique. Sintered (at 1100 °C for 5 h) 2 mm × 5 mm × 10 mm bar samples were mechanically polished and cleaned in ethanol prior to the conductivity test. Currents and voltages were applied and recorded by a source meter (Keithley 2420), which was controlled by the LabVIEW (National Instrument) program.

The electrode polarization resistances based on symmetrical cells were measured between 500 and 750 °C in an ambient air atmosphere using electrochemical impedance spectroscopy (EIS) recorded by the VSP (Bio-Logic) electrochemical workstation. The frequency range for the EIS was 0.01−100 kHz and the signal amplitude was 10 mV under open cell potential (OCP) conditions. The EIS data were analyzed by the ZView 2.9 (Scribner Associates) program.

The oxygen permeability experiments were carried out in a vertical high-temperature gas permeation setup equipped with a gas chromatograph (Varian, CP-3800) to analyze the effluents, as described elsewhere.[35] The gas flowed as the sweep gas at a volumetric rate of 100 mL min^{-1} [STP], and the oxygen-rich side was exposed to ambient atmosphere. The oxygen permeation flux was calculated as described elsewhere.[16,36]

The electrical conductivity relaxation (ECR) method was used to determine the oxygen bulk diffusion coefficient (D_{chem}) and surface exchange coefficient (k_{chem}) of $SrCo_{1-x}Sc_xO_{3-\delta}$, the description of which can be found elsewhere.[37] The configuration and sample characteristics were identical to those used for the electronic conductivity testing. ECRTOOLS was used to estimate both D_{chem} (cm^2 s^{-1}) and k_{chem} (cm s^{-1}) coefficients, check the sensitivity, and quantify the uncertainty in the experiments.[38]

Computation Details. Spin-polarized DFT calculations were performed using the Vienna *ab initio* simulation package (VASP)[39,40]

DOI: 10.1021/acsami.5b00358
ACS Appl. Mater. Interfaces 2015, 7, 8562−8571

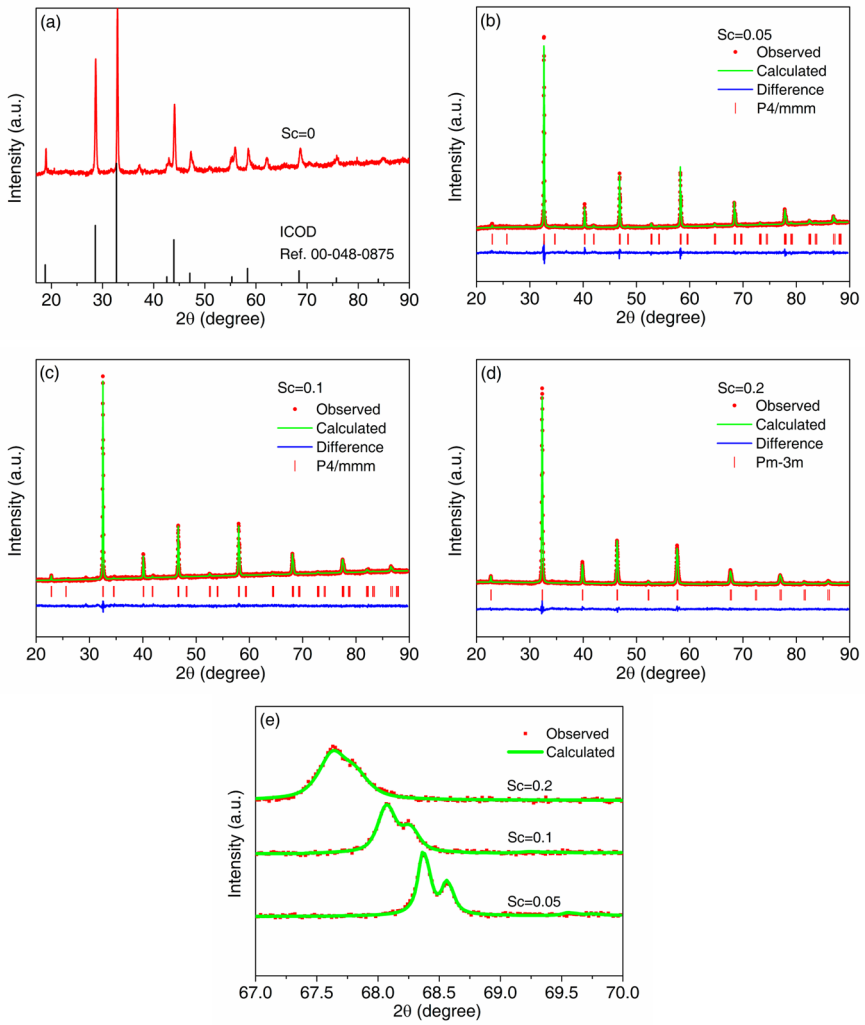

Figure 1. XRD patterns of $SrCoO_{3-\delta}$ (a). XRD patterns and Rietveld refinement data of $SrCo_{0.95}Sc_{0.05}O_{3-\delta}$ (b) and $SrCo_{0.9}Sc_{0.1}O_{3-\delta}$ (c) with the tetragonal structure and *P*4/*mmm* space group, and $SrCo_{0.8}Sc_{0.2}O_{3-\delta}$ (d) with the cubic structure and $Pm\bar{3}m$ space group; magnified XRD patterns of $SrCo_{0.95}Sc_{0.05}O_{3-\delta}$, $SrCo_{0.9}Sc_{0.1}O_{3-\delta}$, and $SrCo_{0.8}Sc_{0.2}O_{3-\delta}$ between 67.0 and 70.0° (2θ) (e).

with the projector-augmented wave (PAW) method[41] and plane wave basis. The exchange correlation functional was considered under the generalized-gradient approximation (GGA) of the Perdew–Burke–Ernzehof (PBE) type.[42] The $4s^2 4p^6 5s^2$ of Sr, $3d^8 4s^1$ of Co, $2s^2 2p^4$ of O, and $3s^2 3p^6 4s^2 3d^1$ of Sc were treated as valence electrons. The DFT+U approach was applied in all the calculations. The Hubbard U parameter for the transition metal Co was set to be 3.3 eV.[43,44] In addition, the O_s pseudopotential was used for oxygen in the VASP potential library. For the tetragonal structure, 2 × 2 × 2 supercells were used, with 40 atoms for each supercell. The initial structure of the tetragonal phase was obtained by elongating the cubic structure in the *c* axis, changing the $Pm\bar{3}m$ cubic symmetry to *P*4/*mmm*. The hexagonal phase, adopting a 2H-$BaNiO_3$-type structure with space group $P6_3/mmc$, was studied using 2 × 2 × 1 supercells, also with 40 atoms in each supercell. The tolerance for the self-consistent electronic steps and the force convergence during relaxation calculations were 10^{-5} eV and 0.02 eV/Å respectively. The kinetic energy cutoff of the plane wave basis was set to 480 eV, and a 4 × 4 × 4 Monkhorst–Pack k-point mesh was adopted for the tetragonal supercell. For the hexagonal supercell, a 3 × 3 × 6 γ-centered k-point mesh was used. We considered only the ferromagnetism (FM) state since the FM state was found to be the ground state for $SrCoO_3$[45] and, besides, the energetic properties of the FM state and antiferromagnetic (AFM) state are typically small.[46,47] In the calculation procedure, all structures were first fully relaxed with changing cell shape and volume; then the defect calculations were conducted with fixed lattice parameters and freely adjustable atom positions. This is because the defect energies do not differ much (0.05 eV) from the calculations with variable lattice parameters.[48] The density of states (DOS) was calculated by doubling the k-point mesh density in each direction and with a tetrahedron smearing method.[49]

The temperature effect was taken into account by considering vibrational energy and entropy. The vibrational frequencies were computed in VASP by the supercell approach, and the free energy was computed using the PHONOPY code.[50] The free energy was then used to investigate the phase transition temperature.[51] The purpose of this result is to illustrate the structural stabilization induced by Sc addition.

RESULTS AND DISCUSSION

Phase Structure and Composition. The phase structures of the as-synthesized $SrCo_{1-x}Sc_xO_{3-\delta}$ powders were determined by XRD with a more detailed analysis undertaken using Rietveld refinement. For the undoped $SrCoO_{3-\delta}$ parent oxide, mainly a 2H-$BaNiO_3$-type hexagonal structure with ordered oxygen vacancies was formed (Figure 1a). While for the doped $SrCo_{0.8}Sc_{0.2}O_{3-\delta}$, the formed structure was characterized as an oxygen-vacancy-disordered cubic crystal structure with the $Pm\bar{3}m$ space group and lattice parameters of $a = b = c = 3.9151$ Å (Figure 1d). These results agree well with that of the

DOI: 10.1021/acsami.5b00358
ACS Appl. Mater. Interfaces 2015, 7, 8562–8571

previous work for samples prepared by the sol−gel process.[9] Analysis of the diffraction peaks shows an increase in splitting with a decrease in the Sc content up to $x = 0.05$ and 0.1 (Figure 1e). This suggests the appearance of a phase transition. These structures, for the description of $SrCo_{1-x}Sc_xO_{3-\delta}$ ($x = 0.05$ and 0.1), may be more precisely described as a tetragonal structure with the $P4/mmm$ space group and with lattice parameters of $a = b = 3.8756$ Å and $c = 3.8808$ Å for $SrCo_{0.95}Sc_{0.05}O_{3-\delta}$, and $a = b = 3.8912$ Å and $c = 3.8954$ Å for $SrCo_{0.9}Sc_{0.1}O_{3-\delta}$. The refinement converged to final reliability R-factors (not corrected for background) of $R_p = 1.23\%$ and $R_{wp} = 1.59\%$ for $SrCo_{0.8}Sc_{0.2}O_{3-\delta}$, $R_p = 1.30\%$ and $R_{wp} = 1.66\%$ for $SrCo_{0.9}Sc_{0.1}O_{3-\delta}$, and $R_p = 1.54\%$ and $R_{wp} = 2.20\%$ for $SrCo_{0.95}Sc_{0.05}O_{3-\delta}$. It should be noted that the phase structures of the $x = 0.05$ and $x = 0.1$ obtained in this work are slightly different from a previous study, in which materials were prepared via sol−gel synthesis and took the cubic perovskite structure.[9] This finding suggests that the preparation method influences the final phase structure of the oxide. The difference in phase structures may largely be due to the distribution of elements during the synthesis. For the solid-state reaction method, partial Sc may be unevenly distributed inside the $SrCoO_{3-\delta}$ lattice, due to the microsized raw materials. Whereas, for the sol−gel process of fabrication, the reactants are homogeneously mixed at the molecular level. It should be pointed out that the preparation method has a negligible effect on the material stoichiometries, since the concentrations of cations in $SrCo_{1-x}Sc_xO_{3-\delta}$ are comparable to the nominal compositions according to the ICP results, where the Sr/Co/Sc ratios are 1.02:1:0, 1.02:0.94:0.05, 1.01:0.89:0.1, and 1:0.79:0.2 for the nominal $SrCoO_{3-\delta}$, $SrCo_{0.95}Sc_{0.05}O_{3-\delta}$, $SrCo_{0.9}Sc_{0.1}O_{3-\delta}$, and $SrCo_{0.8}Sc_{0.2}O_{3-\delta}$, respectively. However, the uneven distribution of the dopant (Sc) may cause the appearance of a negligible secondary phase in $SrCo_{1-x}Sc_xO_{3-\delta}$ when the concentration of dopant is lower than $x = 0.2$. For $SrCo_{0.95}Sc_{0.05}O_{3-\delta}$ and $SrCo_{0.9}Sc_{0.1}O_{3-\delta}$, a negligible peak at ~29° (2θ) may indicate the existence of a secondary phase related to the hexagonal structure, while for $SrCo_{0.8}Sc_{0.2}O_{3-\delta}$, no additional peaks are detected. In addition, the small difference in the fitted a/b and c parameters for the tetragonal structure of $SrCo_{0.95}Sc_{0.05}O_{3-\delta}$ and $SrCo_{0.90}Sc_{0.10}O_{3-\delta}$ suggests that the transition between the two structures is possible. Since both tetragonal and cubic structures are characterized by disordered oxygen vacancies, it can be concluded that a small amount of Sc^{3+} doping efficiently stabilizes the oxygen-disordered phase.

To obtain a fundamental understanding of the structure evolution of the Sc-doped $SrCoO_{3-\delta}$, the free energy difference between the two phases ($\Delta F = F_{tet} - F_{hex}$) was determined as shown in Figure 2. A positive ΔF value corresponds to a more stable hexagonal phase compared to the tetragonal one. For $SrCoO_{3-\delta}$, the free energy difference between the tetragonal phase and the hexagonal phase was calculated as 3.25 eV/supercell at 0 K, suggesting a more stable hexagonal phase than the tetragonal phase. At room temperature, the free energy difference is also positive, indicating a more stable hexagonal phase as well. This is supported by the experimental XRD results as shown in Figure 1, where the diffraction pattern for $SrCoO_{3-\delta}$ revealed a complicated structure consisting predominately of the hexagonal phase. With increasing temperature, the free energy of the tetragonal phase decreased quicker, and a phase transition is predicted to occur at around 1500 K. Interestingly, after Sc B-site doping of only 1/8 in $SrCoO_{3-\delta}$,

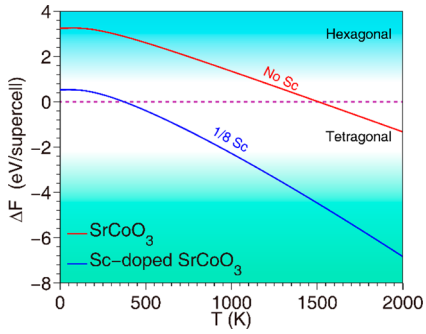

Figure 2. Free energy difference between the tetragonal phase and the hexagonal phase for undoped and Sc-doped $SrCoO_3$.

the calculated phase energy difference dropped significantly to only 0.53 eV/supercell, and the transition temperature decreased to around 350 K. Our calculations support that doping Sc into $SrCoO_{3-\delta}$ is an effective approach to stabilize the oxygen-vacancy-disordered tetragonal structure.

In addition to the compositional elements, oxygen vacancies act as positive charge carriers in the $SrCo_{1-x}Sc_xO_{3-\delta}$ lattice. The oxygen vacancies can have a significant effect on the lattice structure as well as the oxygen kinetics of the oxide. The iodometric titration method was employed to determine the room-temperature oxygen nonstoichiometry of the various oxides. Nonstoichiometries δ of 0.313, 0.311, and 0.310 were found for $SrCo_{0.95}Sc_{0.05}O_{3-\delta}$, $SrCo_{0.9}Sc_{0.1}O_{3-\delta}$, and $SrCo_{0.8}Sc_{0.2}O_{3-\delta}$, respectively. A lower nonstoichiometry δ of 0.234 was found for the undoped $SrCoO_{3-\delta}$ oxide. This finding suggests a correlation between the Sc doping fraction and the resultant oxygen nonstoichiometry for the $SrCoO_{3-\delta}$ oxide. A similar trend was observed for Sb doping in $SrCo_{1-x}Sb_xO_{3-\delta}$ compounds, where the oxygen nonstoichiometry was determined by thermogravimetric analysis under 10% H_2 + 90% N_2 reducing conditions.[11]

For oxides, the surface composition (elements and oxygen vacancies) is usually different from the bulk. For example, strontium segregation is a common phenomenon for Sr-containing perovskite oxides.[52,53] Such segregation may have a significant impact on the ORR activity by blocking the oxygen surface exchange processes. To elucidate the Sc doping effect on the oxide surface, the surface compositions of the $SrCo_{1-x}Sc_xO_{3-\delta}$ series were analyzed by XPS. Figure 3a shows the survey spectra for $SrCo_{1-x}Sc_xO_{3-\delta}$, where the characteristic peaks of Sr, Co, Sc, and O are present. The atomic ratios of 0, 0.059, 0.092, and 0.218 for [Sc]/([Co]+[Sc]) were found respectively for the $SrCoO_{3-\delta}$, $SrCo_{0.95}Sc_{0.05}O_{3-\delta}$, $SrCo_{0.9}Sc_{0.1}O_{3-\delta}$, and $SrCo_{0.8}Sc_{0.2}O_{3-\delta}$ samples. These are reasonably close to the theoretical values. For all samples, a slightly higher atomic ratio for Sr was observed on the surface. This may be attributed to the segregation of Sr to the surface, a common feature of Sr-containing perovskites.[52,53] Interestingly, the degree of Sr surface segregation decreased with an increase in Sc doping content, where the [Sr]/([Sr] + [Co] + [Sc]) ratio decreased from 0.570 for $SrCo_{0.95}Sc_{0.05}O_{3-\delta}$ to 0.518 for $SrCo_{0.8}Sc_{0.2}O_{3-\delta}$, with a theoretical value of 0.5. This suggests that the Sc doping likely suppresses the strontium segregation. Other possible approaches to suppress the Sr surface segregation have also been theoretically proposed.[54] Figure 3b shows the Co 2p core-level spectra of the various $SrCo_{1-x}Sc_xO_{3-\delta}$ samples. The observed doublet peaks located at binding energies of ~780

DOI: 10.1021/acsami.5b00358
ACS Appl. Mater. Interfaces 2015, 7, 8562−8571

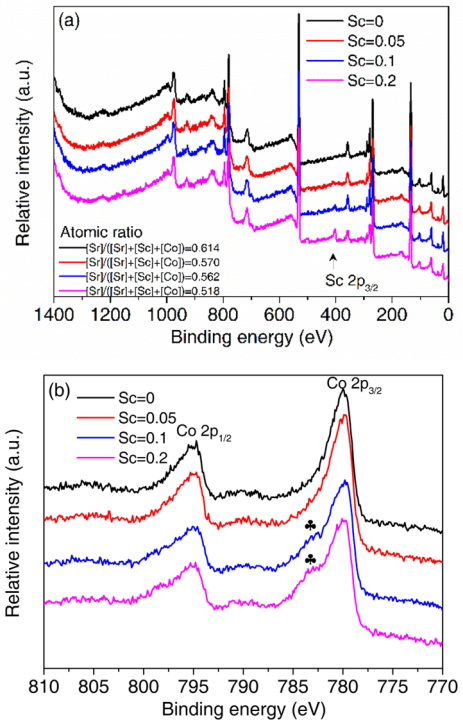

Figure 3. Survey spectra of the $SrCo_{1-x}Sc_xO_{3-\delta}$ series (a) and high-resolution spectra of the Co 2p core level within $SrCo_{1-x}Sc_xO_{3-\delta}$ (b).

and ~795 eV were distinguishable and were associated with the Co $2p_{3/2}$ and Co $2p_{1/2}$, respectively. Satellites at ~790 eV were also observed in the Co core-level spectra. In addition, Co $2p_{3/2}$ spectra contained shoulder peaks at ~783 eV for both $SrCo_{0.9}Sc_{0.1}O_{3-\delta}$ and $SrCo_{0.8}Sc_{0.2}O_{3-\delta}$, suggesting that Sc doping lowered the valence of the surface Co cations.

Charge Transport/Diffusion Properties. The ORR over an MIEC electrode involves both oxygen ion and electron transport/diffusion in the bulk and oxygen exchange at the surface. Sufficient electronic conductivity is required to minimize the ohmic resistance of the electrode. The phase structure and oxidation state of the B-site cations may also impact the electronic conductivity. To understand the effect of Sc doping on the electronic conductivity of $SrCoO_{3-\delta}$, the temperature and oxygen partial pressure dependence on the total electrical conductivities were measured with the results shown in Figure 4. For the undoped $SrCoO_{3-\delta}$ ($x = 0$), an increase in conductivity with temperature was observed, indicating a semiconducting conducting behavior. While for Sc doping with $x \geq 0.05$, a transition from semiconducting to metallic conductivity was observed at intermediate temperatures, with an improved conductivity as compared to undoped $SrCoO_{3-\delta}$. The change in conductivity behavior after doping may originate from the change in the crystal structure. The semiconducting behavior of the undoped $SrCoO_{3-\delta}$ may be related to the hexagonal crystal phase. As previously discussed, a small amount of Sc doping results in the stabilization of the more symmetric tetragonal or cubic phase and therefore a more metallic conductivity. This feature may be attributed to the M−O−M chain (where M is the transition metal). For the cubic and tetragonal structure, the M−O−M angle is close to 180°, and therefore a larger overlap exists between the M 3d electrons and the O 2p electrons, enabling a better electronic conduction. This supports the dramatic increase in conductivity observed by doping 5% Sc into the $SrCoO_{3-\delta}$ lattice. Surprisingly, an increase in doping beyond $x = 0.05$ results in a decrease in the conductivity. This effect can be elucidated by the following DFT analysis.

To obtain a fundamental understanding of the electrical conducting behavior, both the tetragonal $SrCoO_3$ and Sc-doped $SrCoO_3$ phases were investigated by DFT. Projected density of states (PDOS) for the tetragonal undoped and Sc-doped $SrCoO_3$ were calculated and are shown in Figure 5. Both materials exhibited metallic characteristics, as revealed by the nonzero DOS at the Fermi level. Further inspection at the Fermi level indicates that the metallic conductivity is a result of the hybridization between Co and O, which spans the entire valence band. In both plots, Sr does not contribute to the DOS around the Fermi level, suggesting that the A-site cation does not directly influence the conductivity. Comparisons of Figure 5a,b show that the hybridization between Co and O around the Fermi level decreases with the introduction of B-site Sc doping by $x = 0.125$. Furthermore, the Sc cation does not contribute to the valence band maximum. Therefore, it can be expected that with the increase of Sc content, the electronic conductivity of the material decreases. This is in agreement with the experimental results.

Following the DFT study, a defect chemistry model further analyzed the dependence of conductivity on temperature and oxygen partial pressure. We considered a parent ABO_3 perovskite structure where the oxidation states of both A-site and B-site cations are reference at +3.[56] In this model, Co was considered to be in the +3 charge state, Sr in the +2 charge state, Sc in the +3 charge state, and O in the −2 charge state. The Sr site is noted as Sr_A' and an oxygen vacancy as $V_O^{\bullet\bullet}$, where the Krönig−Vink notation is used. As experimentally observed, at a specific temperature the conductivity increased with oxygen partial pressure, which suggests a p-type conductivity. As in the case of a delocalized electron model, a hole is written as $h^{\bullet}$. The active charges within the material are assumed to be $h^{\bullet}$, $V_O^{\bullet\bullet}$, and Sr_A'. The charge balance can be written as

$$p + 2[V_O^{\bullet\bullet}] = [Sr_A'] \quad (1)$$

where p denotes the concentration of holes.

The relation between $h^{\bullet}$ and $V_O^{\bullet\bullet}$ can be described by the reaction

$$2h^{\bullet} + O_O^{\times} = V_O^{\bullet\bullet} + \frac{1}{2}O_2 \quad (2)$$

whose equilibrium constant is

$$K_{eq} = \frac{[V_O^{\bullet\bullet}]pO_2^{1/2}}{p^2[O_O^{\times}]} \quad (3)$$

Combining eqs 1 and 3 gives

$$p(1 + 2K_{eq}[O_O^{\times}]pO_2^{-1/2}p) = [Sr_A'] \quad (4)$$

Under the condition of $1 \gg 2K_{eq}[O_O^{\times}]pO_2{}^{-1/2}p$, we have $p \approx [Sr_A']$, suggesting that the conductivity is insensitive to the oxygen pressure. For localized holes and vacancy-ordered structures, as in the case of $SrCoO_{3-\delta}$, the charge equilibrium can be recast as $[Co_{Co}^{\bullet}] + 2[V_O^{\bullet\bullet}] = [Sr_A']$.[56] In this case, oxygen vacancy ordering is detrimental to the oxygen incorporation, and thus the concentration of $V_O^{\bullet\bullet}$ tends to be insensitive to oxygen partial pressure. This occurs for the undoped material with $x = 0$. If instead $1 \ll 2K_{eq}[O_O^{\times}]pO_2{}^{-1/2}p$, we derive $p \propto K_{eq}^{-1/2}pO_2^{1/4}$. If the equilibrium constant K_{eq} increases with

DOI: 10.1021/acsami.5b00358
ACS Appl. Mater. Interfaces 2015, 7, 8562−8571

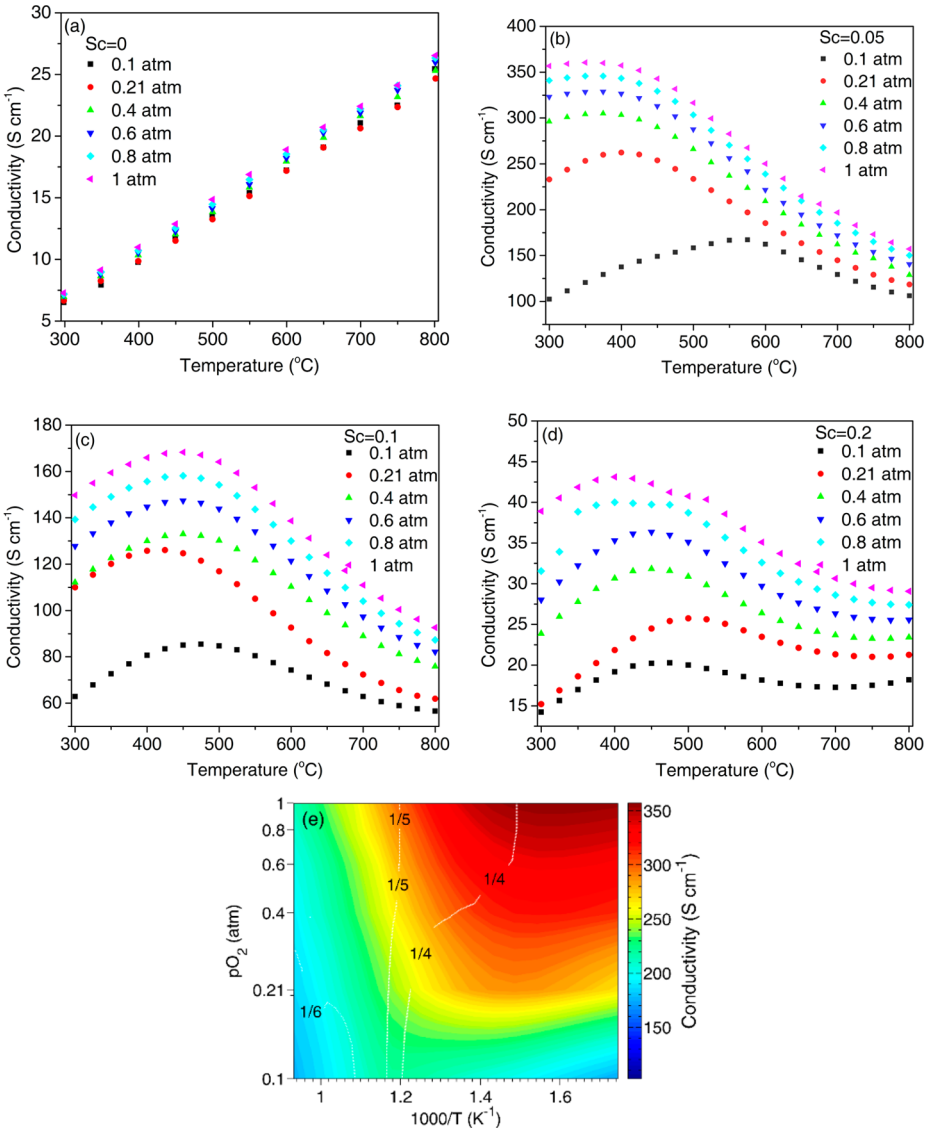

Figure 4. Temperature dependence of electronic conductivities of $SrCoO_{3-\delta}$ (a), $SrCo_{0.95}Sc_{0.05}O_{3-\delta}$ (b), $SrCo_{0.9}Sc_{0.1}O_{3-\delta}$ (c), and $SrCo_{0.8}Sc_{0.2}O_{3-\delta}$ (d) at various oxygen partial pressures. The electronic conductivity map with temperature reciprocal and oxygen partial pressure for $SrCo_{0.95}Sc_{0.05}O_{3-\delta}$ (e). The contour line with fraction number indicates regularized numerical[55] n in the exponential relation $\sigma \propto pO_2^n$.

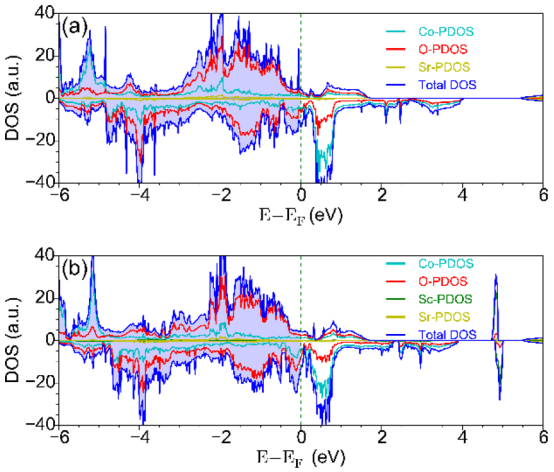

Figure 5. PDOS for undoped tetragonal $SrCoO_3$ (a) and Sc-doped tetragonal $SrCoO_3$ (b).

temperature ($[V_O^{\bullet\bullet}]$ increases with temperature), the hole concentration p and conductivity decrease with temperature.[56] On the other hand, the conductivity will also show exponential dependence on oxygen partial pressure, which is more pronounced at low temperature because of the larger factor $K_{eq}^{-1/2}$. Such conclusions are consistent with our experimental results, as shown in Figure 4e for corresponding to $x = 0.05$.

Further work on the oxygen defect formation energy in relation to the Sc doping effect was undertaken. The oxygen vacancy formation energy was computed using the formula proposed in the work by Lee et al.,[44] where the DFT-computed O_2 overbinding was offset using a correction term. The oxygen vacancy formation energy is found by

$$E_{Vo} = E_{def} + \frac{1}{2}(\Delta h_{cor}^{0} + E_{O_2}^{triplet}) - E_{per} \quad (5)$$

where E_{def} is lattice energy with one oxygen vacancy, $E_{O_2}^{triplet}$ is the computed energy for triplet O_2, E_{per} is the energy for a perfect lattice, and Δh_{cor}^{0} is the energy correction term.

DOI: 10.1021/acsami.5b00358
ACS Appl. Mater. Interfaces 2015, 7, 8562−8571

We employed the same strategy as in the work by Lee et al.[44] and obtained 0.72 eV for the O_2 overbinding correction. Using this method, we computed the oxygen vacancy formation energy of $LaMnO_3$ to be 3.79 eV, which is consistent with the value reported by Lee et al.[44] Oxygen vacancy formation energies in the tetragonal, undoped $SrCoO_3$ were computed to be −0.69 and −0.70 eV (two different O sites). The negative energies indicate that the formation of oxygen vacancy in the tetragonal $SrCoO_3$ is a spontaneous process. This finding consequently implies that the stoichiometric tetragonal $SrCoO_3$ is unstable. The minimum defect energies of corresponding oxygen sites are listed in Table 1.

Table 1. Lowest Oxygen Vacancy Formation Energy at Different Locations

vacancy location	undoped $SrCoO_3$	1/8 Sc-doped $SrCoO_3$
Co−O−Co	−0.70 eV	0.02 eV
Sc−O−Co		0.63 eV

The above calculation results reveal that oxygen vacancies are less favorable to form for the tetragonal B-site Sc doped $SrCoO_{3-\delta}$ oxide. Furthermore, oxygen vacancies are even less favorable for Sc neighboring sites. The increased vacancy formation energy in the Sc−O−Co chain, however, can be explained in relation to the bonding strength between Sc and O. As shown in Figure 6, the charge density difference was

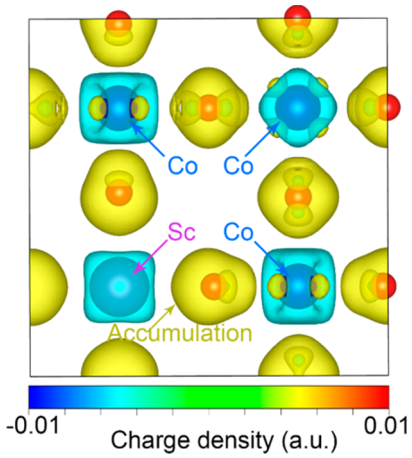

Figure 6. Charge density difference between a self-consistent calculation and the atomic charge.

obtained by subtracting the atomic charge density from that obtained from a self-consistent calculation. From this charge density difference plot, the bonding strength and covalence bond preference can be qualitatively analyzed by inspecting the charge accumulation, shown in yellow and red, or depletion, shown in blue.[57] Analysis of this shows that the bonding strength between Sc and O is higher than that between Co and O, although the interaction does not contribute to the electronic conductivity, as indicated by the increased charge accumulation zone between Sc and O. Therefore, this suggests that the defect formation energy around Sc should be higher. This finding also implies that the oxygen anion may be trapped around the Sc atom. This will result in a reduced oxygen diffusion coefficient with increasing Sc content, as the formation of oxygen vacancies is the first step in oxygen migration based on a vacancy hopping mechanism. For applications as cathodes of SOFCs or membrane materials for oxygen separation, the performance of the $SrCo_{1-x}Sc_xO_{3-\delta}$ series is directly related to the oxygen kinetics. Therefore, the above finding suggests that the Sc doping content should be minimized in order to achieve the highest oxygen kinetics, under the condition that the oxygen-vacancy-disordered structure is effectively stabilized.

The ORR kinetic parameters D_{chem} and k_{chem} of the $SrCo_{1-x}Sc_xO_{3-\delta}$ series were derived from ECR curves. These were analyzed to identify the effect of Sc doping on the material activity as cathodes for SOFC and oxygen permeation rate as materials of OTMs. Figure 7a shows the typical ECR curves of

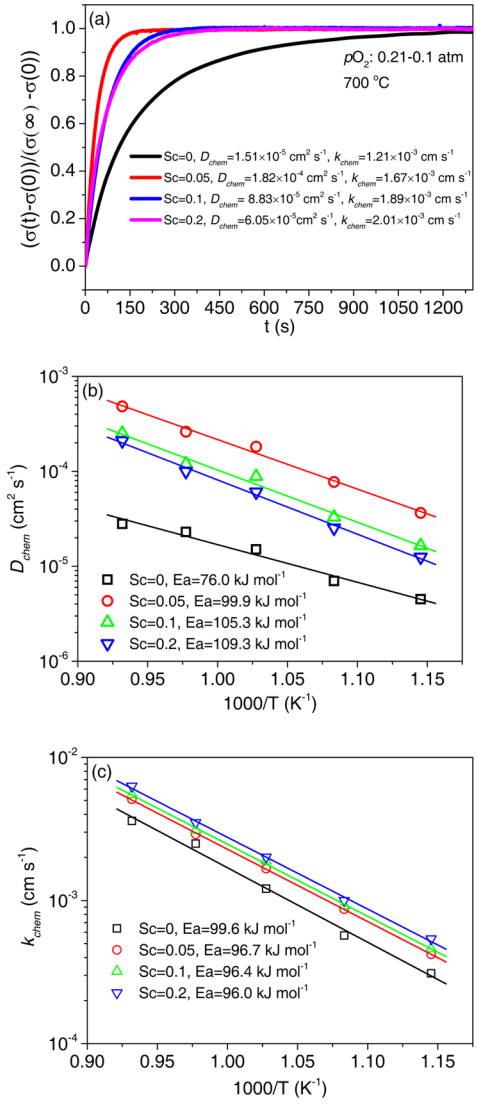

Figure 7. Typical ECR curves of $SrCo_{1-x}Sc_xO_{3-\delta}$ at 700 °C after a sudden change of oxygen partial pressure from 0.21 to 0.1 atm (a). Temperature dependence of the D_{chem} (b) and k_{chem} (c) of $SrCo_{1-x}Sc_xO_{3-\delta}$.

the $SrCo_{1-x}Sc_xO_{3-\delta}$ series, obtained by a sudden change of oxygen partial pressure from 0.21 to 0.1 atm at 700 °C. The derived D_{chem} and k_{chem} values were plotted in the Arrhenius form in Figure 7b,c. Both parameters, D_{chem} and k_{chem}, improved after the doping of Sc into the lattice of $SrCoO_{3-\delta}$, as expected from theoretical calculation. It is promising that the calculated D_{chem} and k_{chem} values of the $SrCo_{1-x}Sc_xO_{3-\delta}$

DOI: 10.1021/acsami.5b00358
ACS Appl. Mater. Interfaces 2015, 7, 8562−8571

composites ($x > 0$) are comparable to those of several advanced perovskite cathodes, such as $Ba_{0.5}Sr_{0.5}Co_{0.8}Fe_{0.2}O_{3-\delta}$ and $Ba_{0.95}La_{0.05}FeO_{3-\delta}$.[37,58,59] *For example*, the calculated D_{chem} and k_{chem} values of $SrCo_{0.95}Sc_{0.05}O_{3-\delta}$ at 700 °C are 1.82×10^{-4} cm^2 s^{-1} and 1.67×10^{-3} cm s^{-1}, respectively. As expected, $SrCo_{0.95}Sc_{0.05}O_{3-\delta}$ showed the highest D_{chem} value among the others. However, k_{chem} values showed a monotonic increase with the Sc doping content and D_{chem} values decreased for $x > 0.05$. As previously outlined, an increase in Sc concentration results in a decrease in oxygen vacancy concentration and electronic conductivity as suggested from the DFT calculation. This may explain the decreased D_{chem} with doping once the stabilization of oxygen-vacancy-disordered structure is reached ($x = 0.05$). The unusual trend of k_{chem} may be related to the degree of Sr segregation (Figure 3b), since the increase of Sr segregation with the decrease of Sc content on the surface may hinder the oxygen surface exchange rate.[52]

ORR Activity. The activities of $SrCo_{1-x}Sc_xO_{3-\delta}$ oxides for ORR at elevated temperatures were first quantified by EIS using symmetrical cells with thin-film $SrCo_{1-x}Sc_xO_{3-\delta}$ electrodes fabricated by PLD. The PLD technique is adopted to alleviate the morphological complexities of the cathode layer and to gain intrinsic properties of materials. To determine the thin-film electrode compositions, the atomic ratio change with sputtering time in depth profiling XPS is shown in Figure 8. Although the

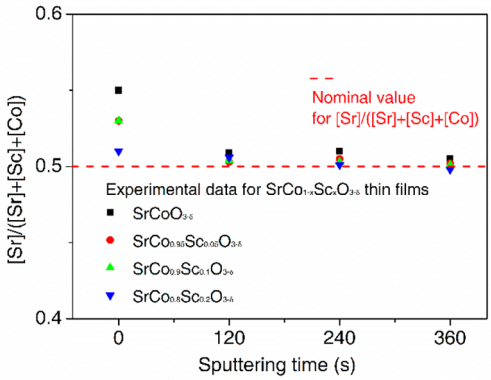

Figure 8. Atomic ratio change of $SrCo_{1-x}Sc_xO_{3-\delta}$ thin films with sputtering time in depth profiling XPS.

Sr segregation at the surface of the thin films prepared by PLD is also observed, it affects only the region up to a few nanometers. Figure 9 shows the Arrhenius representation of the electrode polarization resistance in the temperature range of

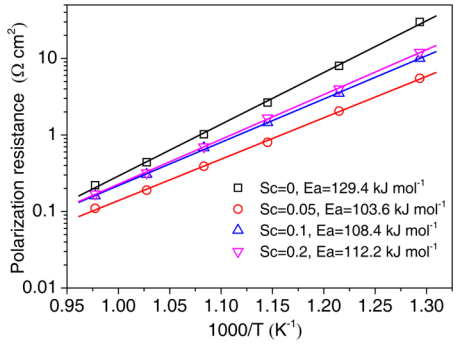

Figure 9. Temperature dependence of the electrode polarization resistances of $SrCo_{1-x}Sc_xO_{3-\delta}$ electrodes.

500−750 °C. Electrode polarization resistances as low as 0.11, 0.16, and 0.17 Ω cm^2 were obtained at 750 °C for $SrCo_{0.95}Sc_{0.05}O_{3-\delta}$, $SrCo_{0.9}Sc_{0.1}O_{3-\delta}$, and $SrCo_{0.8}Sc_{0.2}O_{3-\delta}$, respectively. Furthermore, a resistance of 0.22 Ω cm^2 was observed for the Sc-free $SrCoO_{3-\delta}$. $SrCoO_{3-\delta}$, $SrCo_{0.95}Sc_{0.05}O_{3-\delta}$, $SrCo_{0.9}Sc_{0.1}O_{3-\delta}$, and $SrCo_{0.8}Sc_{0.2}O_{3-\delta}$ exhibited an activation energy (Ea) of 129.4, 103.6, 108.4, and 112.2 kJ mol^{-1}, respectively. As previously discussed, it is suggested that the enhanced ORR activity after doping with Sc results from the stabilization of the oxygen-vacancy-disordered structure. After the stabilization of the oxygen-vacancy-disordered structure, both the polarization resistance and activation energy were found to increase with Sc doping amount. These trends are consistent with previous findings in this work and can be attributed to the decreased oxygen vacancy concentration and electronic conductivity and the increased defect association, with the increase in Sc doping in $SrCo_{1-x}Sc_xO_{3-\delta}$. Very similar trends were also observed in other doped $SrCo_{1-x}M_xO_{3-\delta}$ systems.[11,21,22,26,27] It should be noted that the electrochemical behavior could also be partially affected by the preparation and sintering processes (e.g., microstructural and interfacial differences), current collectors, and electrolyte.[15,32,33,60,61] One must take caution when comparing detailed values from different authors. It is promising here that the electrode polarization resistances of the doped $SrCo_{1-x}Sc_xO_{3-\delta}$ compositions are quite low even in the thin-film (dense) configuration. This suggests potentially high performance when applied as the porous cathode in intermediate-temperature SOFCs.[30]

The ORR activity of $SrCo_{1-x}Sc_xO_{3-\delta}$ was also analyzed by OTM. The temperature dependence of oxygen permeation fluxes through the $SrCo_{1-x}Sc_xO_{3-\delta}$ membranes with fixed thickness (~1 mm) are shown in the temperature range of 700−900 °C in Figure 10. Similar to previous trends, after Sc B-

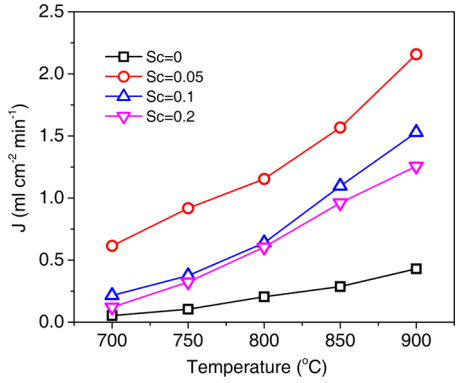

Figure 10. Temperature dependence of oxygen permeation fluxes through $SrCo_{1-x}Sc_xO_{3-\delta}$ membranes.

site substitution by 5% in $SrCoO_{3-\delta}$, the oxygen flux increased dramatically. However, for doping beyond this ($x > 0.05$), the oxygen fluxes of $SrCo_{1-x}Sc_xO_{3-\delta}$ membranes decreased with the further increase of the Sc content in the oxide lattice. Very similar trends were also observed in other doped $SrCo_{1-x}M_xO_{3-\delta}$ and $BaFe_{1-y}M_yO_{3-\delta}$.[23,62,63] Our results support that $SrCo_{0.95}Sc_{0.05}O_{3-\delta}$ has the highest oxygen fluxes at all investigated temperatures (2.16, 1.57, 1.15, 0.919, and 0.615 mL cm^{-2} min^{-1} at 900, 850, 800, 750, and 700 °C), which are much higher than those of undoped $SrCoO_{3-\delta}$ and slightly higher than $SrCo_{0.9}Sc_{0.1}O_{3-\delta}$ and $SrCo_{0.8}Sc_{0.2}O_{3-\delta}$. The oxygen

DOI: 10.1021/acsami.5b00358
ACS Appl. Mater. Interfaces 2015, 7, 8562−8571

fluxes of $SrCo_{0.95}Sc_{0.05}O_{3-\delta}$ are similar to those of BSCF as reported by Shao et al.[64]

CONCLUSIONS

The $SrCo_{1-x}Sc_xO_{3-\delta}$ (x = 0, 0.05, 0.1, and 0.2) series was synthesized by solid-state reaction method and was characterized as possible OTMs and cathodes for SOFCs. Sc doping and doping level at the B site produced pronounced effects on the phase structure, electronic conductivity, defect chemistry, oxygen reduction kinetics, electrode polarization resistance, and oxygen permeability, as revealed by combined experimental study and theoretical calculations. It was found that a stabilization of an oxygen-vacancy-disordered lattice structure was achieved by doping redox-inactive cation, e.g., Sc, into the B site of $SrCoO_{3-\delta}$. In addition, $SrCo_{1-x}Sc_xO_{3-\delta}$ with x = 0.05 showed the highest oxygen fluxes and the lowest electrode polarization resistances. More importantly, these results suggest a universal approach to design efficient and novel MIEC perovskites for SOFCs and OTMs; it is recommend that the optimal dopant amount of the redox-inactive cation should be as slight as possible (typically 5%) for $SrCoO_{3-\delta}$-based materials. That is to stabilize the oxygen-vacancy-disordered phase and ensure high oxygen reduction kinetics.

AUTHOR INFORMATION

Corresponding Authors

*E-mail: francesco.ciucci@ust.hk.

*E-mail: shaozp@njtech.edu.cn.

Author Contributions

#These authors contributed equally to this work. The manuscript was written through contributions of all authors. All authors have given approval to the final version of the manuscript.

Notes

The authors declare no competing financial interest.

ACKNOWLEDGMENTS

This work was supported by the National Science Foundation for Distinguished Young Scholars of China under contract no. 51025209. F.C., D.C., and C.C. thank the Research Grants Council of Hong Kong for support through the projects DAG12EG06 and ECS 639713.

REFERENCES

(1) Shao, Z.; Haile, S. M. A High-Performance Cathode for the Next Generation of Solid-Oxide Fuel Cells. *Nature* **2004**, *431*, 170−173.

(2) Sunarso, J.; Baumann, S.; Serra, J.; Meulenberg, W.; Liu, S.; Lin, Y.; Diniz da Costa, J. Mixed Ionic−Electronic Conducting (MIEC) Ceramic-Based Membranes for Oxygen Separation. *J. Membr. Sci.* **2008**, *320*, 13−41.

(3) Dong, X.; Jin, W.; Xu, N.; Li, K. Dense Ceramic Catalytic Membranes and Membrane Reactors for Energy and Environmental Applications. *Chem. Commun.* **2011**, *47*, 10886−10902.

(4) Zhang, K.; Sunarso, J.; Shao, Z.; Zhou, W.; Sun, C.; Wang, S.; Liu, S. Research Progress and Materials Selection Guidelines on Mixed Conducting Perovskite-Type Ceramic Membranes for Oxygen Production. *RSC Adv.* **2011**, *1*, 1661−1676.

(5) Jeen, H.; Choi, W. S.; Biegalski, M. D.; Folkman, C. M.; Tung, I. C.; Fong, D. D.; Freeland, J. W.; Shin, D.; Ohta, H.; Chisholm, M. F.; Lee, H. N. Reversible Redox Reactions in an Epitaxially Stabilized $SrCoO_x$ Oxygen Sponge. *Nat. Mater.* **2013**, *12*, 1057−1063.

(6) Suntivich, J.; May, K. J.; Gasteiger, H. A.; Goodenough, J. B.; Shao-Horn, Y. A Perovskite Oxide Optimized for Oxygen Evolution Catalysis from Molecular Orbital Principles. *Science* **2011**, *334*, 1383−1385.

(7) Pena, M.; Fierro, J. Chemical Structures and Performance of Perovskite Oxides. *Chem. Rev.* **2001**, *101*, 1981−2018.

(8) Jeen, H.; Bi, Z.; Choi, W. S.; Chisholm, M. F.; Bridges, C. A.; Paranthaman, M. P.; Lee, H. N. Orienting Oxygen Vacancies for Fast Catalytic Reaction. *Adv. Mater.* **2013**, *25*, 6459−6463.

(9) Zeng, P.; Ran, R.; Chen, Z.; Zhou, W.; Gu, H.; Shao, Z.; Liu, S. Efficient Stabilization of Cubic Perovskite $SrCoO_{3-\delta}$ by B-Site Low Concentration Scandium Doping Combined with Sol−Gel Synthesis. *J. Alloys Compd.* **2008**, *455*, 465−470.

(10) Nagai, T.; Ito, W.; Sakon, T. Relationship Between Cation Substitution and Stability of Perovskite Structure in $SrCoO_{3-\delta}$-Based Mixed Conductors. *Solid State Ionics* **2007**, *177*, 3433−3444.

(11) Aguadero, A.; Pérez-Coll, D.; de la Calle, C.; Alonso, J. A.; Escudero, M. J.; Daza, L. $SrCo_{1-x}Sb_xo_{3-\delta}$ Perovskite Oxides as Cathode Materials in Solid Oxide Fuel Cells. *J. Power Sources* **2009**, *192*, 132−137.

(12) Montenegro, M. J.; Döbeli, M.; Lippert, T.; Müller, S.; Weidenkaff, A.; Willmott, P. R.; Wokaun, A. Can Thin Perovskite Film Materials be Applied as Model Systems for Battery Applications? *Appl. Surf. Sci.* **2005**, *247*, 197−203.

(13) Zhou, W.; Ran, R.; Shao, Z. Progress in Understanding and Development of $Ba_{0.5}Sr_{0.5}Co_{0.8}Fe_{0.2}O_{3-\delta}$-Based Cathodes for Intermediate-Temperature Solid-Oxide Fuel Cells: A Review. *J. Power Sources* **2009**, *192*, 231−246.

(14) Kuklja, M. M.; Kotomin, E. A.; Merkle, R.; Mastrikov, Y. A.; Maier, J. Combined Theoretical and Experimental Analysis of Processes Determining Cathode Performance in Solid Oxide Fuel Cells. *Phys. Chem. Chem. Phys.* **2013**, *15*, 5443−5471.

(15) Chen, Y.; Wang, F.; Chen, D.; Dong, F.; Park, H. J.; Kwak, C.; Shao, Z. Role of Silver Current Collector on the Operational Stability of Selected Cobalt-Containing Oxide Electrodes for Oxygen Reduction Reaction. *J. Power Sources* **2012**, *210*, 146−153.

(16) Zhang, Z.; Chen, D.; Gao, Y.; Yang, G.; Dong, F.; Chen, C.; Ciucci, F.; Shao, Z. A CO_2-Tolerant Nanostructured Layer for Oxygen Transport Membranes. *RSC Adv.* **2014**, *4*, 25924−25932.

(17) Mueller, D. N.; De Souza, R. A.; Yoo, H.-I.; Martin, M. Phase Stability and Oxygen Nonstoichiometry of Highly Oxygen-Deficient Perovskite-Type Oxides: A Case Study of $(Ba,Sr)(Co,Fe)O_{3-\delta}$. *Chem. Mater.* **2011**, *24*, 269−274.

(18) Chen, D.; Yang, G.; Ciucci, F.; Tade, M. O.; Shao, Z. 3D Core-Shell Architecture from Infiltration and Beneficial Reactive Sintering as Highly Efficient and Thermally Stable Oxygen Reduction Electrode. *J. Mater. Chem. A* **2014**, *2*, 1284−1293.

(19) Deng, Z. Q.; Yang, W. S.; Liu, W.; Chen, C. S. Relationship between Transport Properties and Phase Transformations in Mixed-Conducting Oxides. *J. Solid State Chem.* **2006**, *179*, 362−369.

(20) Aguadero, A.; Alonso, J. A.; Pérez-Coll, D.; de la Calle, C.; Fernández-Díaz, M. T.; Goodenough, J. B. $SrCo_{0.95}Sb_{0.05}O_{3-\delta}$ as Cathode Material for High Power Density Solid Oxide Fuel Cells. *Chem. Mater.* **2009**, *22*, 789−798.

(21) Aguadero, A.; Pérez-Coll, D.; Alonso, J.; Skinner, S.; Kilner, J. A New Family of Mo-Doped $SrCoO_{3-\delta}$ Perovskites for Application in Reversible Solid State Electrochemical Cells. *Chem. Mater.* **2012**, *24*, 2655−2663.

(22) Yang, W.; Hong, T.; Li, S.; Ma, Z.; Sun, C.; Xia, C.; Chen, L. Perovskite $Sr_{1-x}Ce_xCoO_{3-\delta}$ ($0.05 \le X \le 0.15$) as Superior Cathodes for Intermediate Temperature Solid Oxide Fuel Cells. *ACS Appl. Mater. Interfaces* **2013**, *5*, 1143−1148.

(23) Zhang, K.; Ran, R.; Ge, L.; Shao, Z.; Jin, W.; Xu, N. Systematic Investigation on New $SrCo_{1-y}Nb_yO_{3-\delta}$ Ceramic Membranes with High Oxygen Semi-Permeability. *J. Membr. Sci.* **2008**, *323*, 436−443.

(24) Zeng, P.; Shao, Z.; Liu, S.; Xu, Z. P. Influence of M Cations on Structural, Thermal and Electrical Properties of New Oxygen Selective Membranes Based on $SrCo_{0.95}M_{0.05}O_{3-\delta}$ Perovskite. *Sep. Purif. Technol.* **2009**, *67*, 304−311.

DOI: 10.1021/acsami.5b00358
ACS Appl. Mater. Interfaces 2015, 7, 8562−8571

(25) Chen, X.; Huang, L.; Wei, Y.; Wang, H. Tantalum Stabilized $SrCoO_{3-\delta}$ Perovskite Membrane for Oxygen Separation. *J. Membr. Sci.* **2011**, *368*, 159−164.
(26) Shen, Y.; Wang, F.; Ma, X.; He, T. $SrCo_{1-y}Ti_yO_{3-\delta}$ as Potential Cathode Materials for Intermediate-Temperature Solid Oxide Fuel Cells. *J. Power Sources* **2011**, *196*, 7420−7425.
(27) Wang, F.; Zhou, Q.; He, T.; Li, G.; Ding, H. Novel $SrCo_{1-y}Nb_yO_{3-\delta}$ Cathodes for Intermediate-Temperature Solid Oxide Fuel Cells. *J. Power Sources* **2010**, *195*, 3772−3778.
(28) Zhou, W.; Sunarso, J.; Zhao, M.; Liang, F.; Klande, T.; Feldhoff, A. A Highly Active Perovskite Electrode for the Oxygen Reduction Reaction Below 600 °C. *Angew. Chem., Int. Ed.* **2013**, *52*, 14036−14040.
(29) Liang, F.; Zhou, W.; Zhu, Z. A Highly Stable and Active Hybrid Cathode for Low-Temperature Solid Oxide Fuel Cells. *ChemElectroChem.* **2014**, *1*, 1627−1631.
(30) Zhou, W.; Shao, Z.; Ran, R.; Cai, R. Novel $SrSc_{0.2}Co_{0.8}O_{3-\delta}$ as a Cathode Material for Low Temperature Solid-Oxide Fuel Cell. *Electrochem. Commun.* **2008**, *10*, 1647−1651.
(31) Li, X.; Zhao, H.; Gao, F.; Chen, N.; Xu, N. La and Sc Co-Doped $SrTiO_3$ as Novel Anode Materials for Solid Oxide Fuel Cells. *Electrochem. Commun.* **2008**, *10*, 1567−1570.
(32) Wang, F.; Chen, D.; Shao, Z. Composition and Microstructure Optimization and Operation Stability of Barium Deficient $Ba_{1-x}Co_{0.7}Fe_{0.2}Nb_{0.1}O_{3-\delta}$ Perovskite Oxide Electrodes. *Electrochim. Acta* **2013**, *103*, 23−31.
(33) Chen, D.; Yang, G.; Shao, Z.; Ciucci, F. Nanoscaled Sm-Doped CeO_2 Buffer Layers for Intermediate-Temperature Solid Oxide Fuel Cells. *Electrochem. Commun.* **2013**, *35*, 131−134.
(34) Chen, D.; Chen, C.; Dong, F.; Shao, Z.; Ciucci, F. Cobalt-Free Polycrystalline $Ba_{0.95}La_{0.05}FeO_{3-\delta}$ Thin Films as Cathodes for Intermediate-Temperature Solid Oxide Fuel Cells. *J. Power Sources* **2014**, *250*, 188−195.
(35) Zeng, P.; Chen, Z.; Zhou, W.; Gu, H.; Shao, Z.; Liu, S. Re-Evaluation of $Ba_{0.5}Sr_{0.5}Co_{0.8}Fe_{0.2}O_{3-\delta}$ Perovskite as Oxygen Semi-Permeable Membrane. *J. Membr. Sci.* **2007**, *291*, 148−156.
(36) Zhang, Z.; Chen, D.; Chen, Y.; Hao, Y.; Tade, M. O.; Shao, Z. Facile Fabrication and Improved Carbon Dioxide Tolerance of a Novel Bilayer-Structured Ceramic Oxygen Permeating Membrane. *J. Membr. Sci.* **2014**, *472*, 10−18.
(37) Chen, D.; Shao, Z. Surface Exchange and Bulk Diffusion Properties of $Ba_{0.5}Sr_{0.5}Co_{0.8}Fe_{0.2}O_{3-\delta}$ Mixed Conductor. *Int. J. Hydrogen Energy* **2011**, *36*, 6948−6956.
(38) Ciucci, F. Electrical Conductivity Relaxation Measurements: Statistical Investigations Using Sensitivity Analysis, Optimal Experimental Design and Ecrtools. *Solid State Ionics* **2013**, *239*, 28−40.
(39) Kresse, G.; Furthmüller, J. Efficient Iterative Schemes for Ab Initio Total-Energy Calculations Using a Plane-Wave Basis Set. *Phys. Rev. B* **1996**, *54*, 11169−11186.
(40) Kresse, G.; Furthmüller, J. Efficiency of Ab-Initio Total Energy Calculations for Metals and Semiconductors Using a Plane-Wave Basis Set. *Comput. Mater. Sci.* **1996**, *6*, 15−50.
(41) Blöchl, P. E. Projector Augmented-Wave Method. *Phys. Rev. B* **1994**, *50*, 17953−17979.
(42) Perdew, J. P.; Burke, K.; Ernzerhof, M. Generalized Gradient Approximation Made Simple. *Phys. Rev. Lett.* **1996**, *77*, 3865.
(43) Wang, L.; Maxisch, T.; Ceder, G. Oxidation Energies of Transition Metal Oxides within the GGA+U Framework. *Phys. Rev. B* **2006**, *73*, 195107.
(44) Lee, Y.-L.; Kleis, J.; Rossmeisl, J.; Morgan, D. Ab Initio Energetics of $LaBO_3$(001) (B=Mn, Fe, Co, and Ni) for Solid Oxide Fuel Cell Cathodes. *Phys. Rev. B* **2009**, *80*, 224101.
(45) Ali, Z.; Ahmad, I. Band Profile Comparison of the Cubic Perovskites $CaCoO_3$ and $SrCoO_3$. *J. Electron. Mater.* **2013**, *42*, 438−444.
(46) Choi, Y.; Mebane, D. S.; Lin, M.; Liu, M. Oxygen Reduction on $LaMnO_3$-Based Cathode Materials in Solid Oxide Fuel Cells. *Chem. Mater.* **2007**, *19*, 1690−1699.
(47) Kotomin, E. A.; Mastrikov, Y. A.; Heifets, E.; Maier, J. Adsorption of Atomic and Molecular Oxygen on the $LaMnO_3$(001) Surface: Ab Initio Supercell Calculations and Thermodynamics. *Phys. Chem. Chem. Phys.* **2008**, *10*, 4644−4649.
(48) Kotomin, E.; Mastrikov, Y. A.; Kuklja, M.; Merkle, R.; Roytburd, A.; Maier, J. First Principles Calculations of Oxygen Vacancy Formation and Migration in Mixed Conducting $Ba_{0.5}Sr_{0.5}Co_{1-y}Fe_yO_{3-\delta}$ Perovskites. *Solid State Ionics* **2011**, *188*, 1−5.
(49) Blöchl, P. E.; Jepsen, O.; Andersen, O. K. Improved Tetrahedron Method for Brillouin-Zone Integrations. *Phys. Rev. B* **1994**, *49*, 16223.
(50) Togo, A.; Oba, F.; Tanaka, I. First-Principles Calculations of the Ferroelastic Transition between Rutile-Type and $CaCl_2$-Type SiO_2 at High Pressures. *Phys. Rev. B* **2008**, *78*, 134106.
(51) Kim, J.-S.; Yeon, D.-H.; Jung, D. W.; Kwak, C. A Highly Active and Long-Term Stable La-Doped $Ba_xSr_{1-x}Co_{1-y}Fe_yO_{3-\delta}$ Cathode for Solid-Oxide Fuel Cells. *J. Power Sources* **2014**, *249*, 66−71.
(52) Jung, W.; Tuller, H. L. Investigation of Surface Sr Segregation in Model Thin Film Solid Oxide Fuel Cell Perovskite Electrodes. *Energy Environ. Sci.* **2012**, *5*, 5370−5378.
(53) Chen, Y.; Jung, W.; Cai, Z.; Kim, J. J.; Tuller, H. L.; Yildiz, B. Impact of Sr Segregation on the Electronic Structure and Oxygen Reduction Activity of $SrTi_{1-x}Fe_xO_3$ Surfaces. *Energy Environ. Sci.* **2012**, *5*, 7979−7988.
(54) Ding, H.; Virkar, A. V.; Liu, M.; Liu, F. Suppression of Sr Surface Segregation in $La_{1-x}Sr_xCo_{1-y}Fe_yO_{3-\delta}$: A First Principles Study. *Phys. Chem. Chem. Phys.* **2013**, *15*, 489−496.
(55) Bardow, A. Optimal Experimental Design of Ill-Posed Problems: The METER Approach. *Comput. Chem. Eng.* **2008**, *32*, 115−124.
(56) Petrov, A.; Kononchuk, O.; Andreev, A.; Cherepanov, V.; Kofstad, P. Crystal Structure, Electrical and Magnetic Properties of $La_{1-x}Sr_xCoO_{3-\delta}$. *Solid State Ionics* **1995**, *80*, 189−199.
(57) Pavone, M.; Ritzmann, A. M.; Carter, E. A. Quantum-Mechanics-Based Design Principles for Solid Oxide Fuel Cell Cathode Materials. *Energy Environ. Sci.* **2011**, *4*, 4933−4937.
(58) Chen, C.; Chen, D.; Gao, Y.; Shao, Z.; Ciucci, F. Compuational and Experimental Analysis of $Ba_{0.95}La_{0.05}FeO_{3-\delta}$ as a Cathode Material for Solid Oxide Fuel Cells. *J. Mater. Chem. A* **2014**, *2*, 14154−14163.
(59) Dong, F.; Chen, D.; Chen, Y.; Zhao, Q.; Shao, Z. La-Doped $BaFeO_{3-\delta}$ Perovskite as a Cobalt-Free Oxygen Reduction Electrode for Solid Oxide Fuel Cells with Oxygen-Ion Conducting Electrolyte. *J. Mater. Chem.* **2012**, *22*, 15071−15079.
(60) Guo, Y.; Zhou, Y.; Chen, D.; Shi, H.; Ran, R.; Shao, Z. Significant Impact of the Current Collection Material and Method on the Performance of $Ba_{0.5}Sr_{0.5}Co_{0.8}Fe_{0.2}O_{3-\delta}$ Electrodes in Solid Oxide Fuel Cells. *J. Power Sources* **2011**, *196*, 5511−5519.
(61) Chen, D.; Wang, F.; Shao, Z. Interlayer-Free Electrodes for IT-SOFCs by Applying Co_3O_4 as Sintering Aid. *Int. J. Hydrogen Energy* **2012**, *37*, 11946−11954.
(62) Xu, D.; Dong, F.; Chen, Y.; Zhao, B.; Liu, S.; Tade, M. O.; Shao, Z. Cobalt-Free Niobium-Doped Barium Ferrite as Potential Materials of Dense Ceramic Membranes for Oxygen Separation. *J. Membr. Sci.* **2014**, *455*, 75−82.
(63) Kida, T.; Yamasaki, A.; Watanabe, K.; Yamazoe, N.; Shimanoe, K. Oxygen-Permeable Membranes Based on Partially B-Site Substituted $BaFe_{1-y}M_yO_{3-\delta}$(M=Cu or Ni). *J. Solid State Chem.* **2010**, *183*, 2426−2431.
(64) Chen, Y.; Qian, B.; Li, S.; Jiao, Y.; Tade, M. O.; Shao, Z. The Influence of Impurity Ions on the Permeation and Oxygen Reduction Properties of $Ba_{0.5}Sr_{0.5}Co_{0.8}Fe_{0.2}O_{3-\delta}$ Perovskite. *J. Membr. Sci.* **2014**, *449*, 86−96.

DOI: 10.1021/acsami.5b00358
ACS Appl. Mater. Interfaces 2015, 7, 8562−8571